JOURNAL OF SYNCHROTRON RADIATION
ISSN 1600-5775

Self-assembly of block copolymers under non-isothermal annealing conditions as revealed by grazing-incidence small-angle X-ray scattering

Marta Fernández-Regúlez,[a,b] Eduardo Solano,[c] Laura Evangelio,[a,d] Steven Gottlieb,[a] Christian Pinto-Gómez,[a] Gemma Rius,[a] Jordi Fraxedas,[d] Edgar Gutiérrez-Fernández,[e] Aurora Nogales,[e] Mari Cruz García-Gutiérrez,[e] Tiberio A. Ezquerra[e] and Francesc Pérez-Murano[a]*

[a]Instituto de Microelectrónica de Barcelona, IMB-CNM (CSIC), Campus UAB, Bellaterra, Barcelona 08193, Spain, [b]Universitat Autònoma de Barcelona, Bellaterra 08193, Spain, [c]NCD-SWEET Beamline, ALBA Synchrotron Light Source, Cerdanyola del Vallès, Barcelona 08290, Spain, [d]Catalan Institute of Nanoscience and Nanotechnology (ICN2), CSIC and BIST, Bellaterra 08193, Spain, and [e]Instituto de Estructura de la Materia (IEM-CSIC), Serrano 121, Madrid 28006, Spain. *Correspondence e-mail: francesc.perez@csic.es

Received 5 March 2020
Accepted 17 July 2020

Edited by U. Jeng, NSRRC, Taiwan

Keywords: block copolymer; self-assembly; kinetics; correlation length; GISAXS.

Supporting information: this article has supporting information at journals.iucr.org/s

An accurate knowledge of the parameters governing the kinetics of block copolymer self-assembly is crucial to model the time- and temperature-dependent evolution of pattern formation during annealing as well as to predict the most efficient conditions for the formation of defect-free patterns. Here, the self-assembly kinetics of a lamellar PS-*b*-PMMA block copolymer under both isothermal and non-isothermal annealing conditions are investigated by combining grazing-incidence small-angle X-ray scattering (GISAXS) experiments with a novel modelling methodology that accounts for the annealing history of the block copolymer film before it reaches the isothermal regime. Such a model allows conventional studies in isothermal annealing conditions to be extended to the more realistic case of non-isothermal annealing and prediction of the accuracy in the determination of the relevant parameters, namely the correlation length and the growth exponent, which define the kinetics of the self-assembly.

1. Introduction

The self-assembly of block copolymer (BCP) thin films has gained interest during the last decade due to its application as a complementary process for nanostructuring surfaces (Jeong *et al.*, 2013; Bates *et al.*, 2014). In particular, BCP-based large-area patterning can reliably achieve sub-20 nm resolution at low cost and with process simplicity. Pursuing its ultimate development in terms of resolution, defectivity and process integration would allow its implementation in the next technological nodes.

BCPs are composed of two (or more) homopolymer chains, whose blocks are chemically distinct while linked through a covalent bond (Bates & Fredrickson, 1990). When the repulsive interaction between blocks is high enough, a phase separation can be induced by thermal or solvent annealing (Jung & Ross, 2009). Different structural nanodomains, such as lamellae, cylinders or spheres, can be obtained depending on the degree of interaction among the polymer chains, which is quantified by the Flory Huggins interaction parameter, χ, plus the number of monomers, N, and the volume fraction of each block, f. However, self-assembled nanopatterns usually present a random orientation and short order domains. To overcome this limitation, directed self-assembly (DSA) combines standard lithography techniques to create topo-

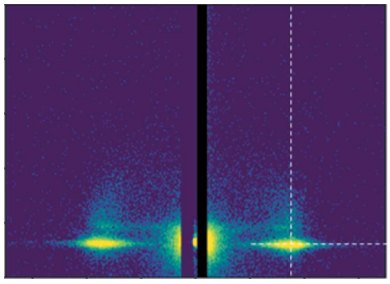

graphical [grapho-epitaxy (Gottlieb, Kazazis *et al.*, 2018)] or chemical [chemo-epitaxy (Fernández-Regúlez *et al.*, 2014; Evangelio *et al.*, 2019)] guiding patterns, so that a specific orientation and position of the BCP self-assembled structures can be obtained (Hu *et al.*, 2014). DSA of BCPs is still considered by the semiconductor industry as a complementary approach to conventional photolithography and patterning towards improving parameters such as resolution, throughput or line edge roughness (IRDS, 2018). Nevertheless, its incorporation in fabrication processes requires the consolidation of multiple parameters such as defectivity, compatibility of self-assembly process conditions, kinetics and throughput among others (Marencic & Register, 2010; Tseng & Darling, 2010; Li & Müller, 2016).

An understanding of the parameters governing the kinetics of the BCP self-assembly process is of key importance to model the evolution of the system as it can be crucial to predict the final order and determine the processing conditions to obtain defect-free patterned areas (Harrison *et al.*, 2002; Murphy *et al.*, 2015; Kim *et al.*, 2014). Both the self-assembly kinetics and obtained morphology have been widely investigated as a function of different physical/experimental parameters (Ji *et al.*, 2011) such as annealing conditions (Berry *et al.*, 2007; Sanz *et al.*, 2011; Majewski & Yager, 2015; Gu *et al.*, 2014), BCP thickness (Black *et al.*, 2017) and BCP/substrate interaction (Harrison, Chaikin *et al.*, 2000). Typically, the characterization of BCP thin films is addressed by using microscopy techniques. In particular, scanning electron microscopy (SEM) (Harrison *et al.*, 2004; Ferrarese Lupi *et al.*, 2013; Perego *et al.*, 2014), atomic force microscopy (AFM) (Magerle, 2000; Hahm & Sibener, 2001; Berry *et al.*, 2007; Chandra *et al.*, 2019) and transmission electron microscopy (TEM) (Segal-Peretz *et al.*, 2015) have been extensively used. However, despite their high spatial resolution, they only provide information about the material surface, as in the case of SEM and AFM, and they are typically limited to surveying small areas. Therefore, conventional topographical characterization of self-assembled BCP layers taken at different sample positions offers limited possibility for statistical analysis of pattern quality and defectivity, and its evaluation is time consuming. Moreover, *in situ* and real-time characterization of the time evolution of the system is limited because of the time resolution inherent to microscopy methods and the incompatibility of equipment with the required harsh conditions involved in the sample processing. In this scenario, grazing-incidence small-angle X-ray scattering (GISAXS) with synchrotron radiation plays a pivotal role to complement the evaluation provided by standard microscopy techniques (Müller-Buschbaum, 2016; Soccio *et al.*, 2014; Rueda *et al.*, 2012; Gottlieb, Rösner *et al.*, 2018), due to the fact that GISAXS probes a sample area that can be several orders of magnitude larger, typically square millimetres, than that explored by microscopy techniques, thanks to the glancing X-ray beam and hence large footprint. Moreover, the collected information is not limited to the polymer surface (Ferrarese Lupi *et al.*, 2017) but also includes some sample volume because of the X-ray penetration into the material, which can be controlled by the incidence angle. This feature opens the possibility for statistical analysis of large areas while having access to information from the entire depth of the film (Müller-Buschbaum, 2016). In addition, GISAXS set-ups often allow the experiments to be performed in a wide range of sample environments and configurations, *e.g.* high-temperature, vacuum, controlled atmosphere conditions *etc.*, making it possible to perform *in situ* and real-time experiments such as solvent and thermal annealing of BCPs.

Remarkably, due to the recent progress in synchrotron instrumentation for GISAXS, sub-millisecond time-resolution measurements can be performed, thus enabling an accurate study of the kinetics of the BCP self-assembly process. However, most of the reported *in situ* and real-time studies using synchrotron radiation were performed on solvent-annealed samples (Papadakis *et al.*, 2008; Di *et al.*, 2010; Gu *et al.*, 2014; Zhang *et al.*, 2014; Sinturel *et al.*, 2014; Berezkin *et al.*, 2018; Lee *et al.*, 2019). In general, the characterization of thermally annealed samples is mainly performed on already self-assembled *ex situ* samples by taking snapshots during the process of interest (Ferrarese Lupi *et al.*, 2017), while only a few studies have been performed during the thermal annealing (Yager *et al.*, 2009; Sepe *et al.*, 2011; Maret *et al.*, 2014; Samant *et al.*, 2016).

In this paper, we report on the self-assembly process of lamellar block copolymer poly (styrene-*block*-methyl-metacrylate), PS-*b*-PMMA, thin films. The spin-coated/deposited BCP thin films were investigated by means of synchrotron GISAXS during thermal annealing (*i.e. in situ*) which consisted of either isothermal or non-isothermal conditions, and in particular during heating ramps at different heating rates. Real-time monitoring has allowed us to investigate the evolution of the pitch as well as the BCP correlation length, thus making it possible to determine the basic kinetics mechanism of the self-assembly process for the complete set of investigated samples. In fact, different from classical modelling, normally limited to isothermal annealing, our study has been extended to and provides predictions for systems with diverse initial sample conditions including: (i) unknown previous annealing history and (ii) pre-annealing evaporation of the solvent at low temperature. In addition, dedicated data analysis enables us to predict the evolution of the system under arbitrary non-isothermal annealing conditions. The model successfully predicts the evolution of the correlation length during the heating ramp. When the final target temperature has been reached after the heating ramp, the evolution during the isothermal annealing is modelled considering the previous evolution of the self-assembly.

2. Experimental

2.1. Materials and sample preparation

Lamellar PS-*b*-PMMA [50:50, molecular weight M_n = 79 kg mol^{-1} and PDI (polydispersity index) = 1.09] BCP and its associated neutral layer (same wetting affinity for both BCP blocks) PS-*r*-PMMA (molecular weight 7.9 kg mol^{-1}, 58 wt%

PS and 42% PMMA and PDI = 1.85) were provided by Arkema. Both polymers were dissolved in propylene glycol monomethyl ether acetate (PGMEA) solvent at 1.5% in weight.

Samples were prepared on 2 cm × 2 cm substrates from silicon wafers (p-type doped, ⟨100⟩ oriented and 4–40 Ω cm^{-1}). First, the substrates were conditioned by exposure to an oxygen plasma at 500 W for 10 min. Then, a thin layer of PS-*r*-PMMA was spin-coated (2000 rpm for 30 s) on the surface and annealed at 230°C in air for 10 min for grafting. The un-grafted polymer chains were removed by dipping the sample in an ultrasonic bath with PGMEA solvent for 1 min. Finally, the BCP, PS-*b*-PMMA, was spin-coated at 2500 rpm and immediately placed on the GISAXS sample holder to perform *in situ* thermal annealing characterization to monitor the self-assembly process. Due to the employed annealing conditions and the surface brush functionalization, perpendicular oriented lamellar structures with a period of 38 nm were formed (Gottlieb *et al.*, 2017; Lorenzoni *et al.*, 2017).

2.2. Sample characterization

In situ GISAXS measurements were carried out at the NCD-SWEET beamline at the ALBA Synchrotron (Cerdanyola del Vallès, Spain) during two separate campaigns/sets of experiments. An X-ray beam of 12.4 keV was set using a Si(111) channel-cut monochromator. Then, the beam was collimated using an array of Be lenses, obtaining a beam size of 475 × 340 µm (H × V) at the sample position. The scattered radiation was recorded with a Pilatus3 S 1M detector (Dectris, Switzerland), which consists of an array of 981 × 1043 (H × V) pixels of 172 µm × 172 µm (H × V). The sample-to-detector distance was 4046 mm for a first set, and 6036 mm for the second round of experiments. The sample-to-detector distance, as well as the reciprocal space, was calibrated using a silver behenate sample for calibration. The X-ray incident angle employed was 0.15°, which corresponds to the critical angle of the Si substrate for the set energy, ensuring minimum penetration and high surface sensitivity.

An adapted Linkam TMS600 film heating stage (accuracy 0.01°C) for grazing-incidence experiments was employed for the *in situ* annealing experiments. Sample temperature was corrected by a calibration curve previously obtained. A protective N_2 atmosphere was used during the experiments. For the isothermal annealing, the samples were first placed at room temperature on the heating stage and then heated to the target annealing temperature (from 160 to 200°C) using a heating ramp of up to 50°C min^{-1} without being exposed to X-rays. GISAXS patterns during the isothermal experiments were collected at the (final) target temperature. On the other hand, samples for the study of non-isothermal treatments were annealed from room temperature to 180°C using different heating rates (5, 10 and 20°C min^{-1}), followed by a dwell time at the maximum temperature of 10 min. In this case, GISAXS patterns were periodically taken during both transient phases, the heating ramp and the steady phase, *i.e.* the isothermal annealing.

2.3. GISAXS analysis

Prior to the *in situ* experiments, the radiation damage induced by the beam on the BCPs was evaluated at different temperatures (see Fig. S1 in the supporting information). We determined that a total sample exposure to the X-rays higher than 1.2 s induced significant damage to the sample, especially at temperatures above the polymer glass transition. Therefore, the GISAXS pattern acquisition time was limited to 30 frames per sample with an integration time of 37 ms, limiting the sample beam damage while obtaining an adequate signal-to-noise ratio for the recorded GISAXS 2D patterns. To guarantee experimental reproducibility, each experiment was repeated at least three times.

Fig. 1 presents a scheme of the geometric configuration of the GISAXS experiments specifying all relevant dimensions. The scattering vector (q) is defined as a function of the incident X-ray beam angle (α_i) and the out-of-plane (α) and in-plane (ω) exit angles:

$$\begin{aligned} q_x &= k_0(\cos\omega\cos\alpha - \cos\alpha_i), \\ q_y &= k_0(\sin\omega\cos\alpha), \\ q_z &= k_0(\sin\alpha_i + \sin\alpha), \end{aligned} \tag{1}$$

where $k_0 = 2\pi/\lambda$ is the wavevector of the incident X-ray beam of wavelength λ (Renaud *et al.*, 2009).

One example of the 2D-GISAXS patterns obtained during isothermal annealing is shown in Fig. 2. Typically, the patterns exhibit a primary diffraction maximum at a certain position ($q_{y,\mathrm{pos}}$, $q_{z,\mathrm{pos}}$) which is associated with the BCP period in perpendicularly oriented lamellar structures (L_0). The recorded 2D-GISAXS patterns were analysed by an in-house-developed software based on MATLAB. 2D-to-1D data reduction consisted of horizontal line cuts (along q_y) at the position of the main diffraction maximum ($q_{z,\mathrm{pos}}$, *circa*

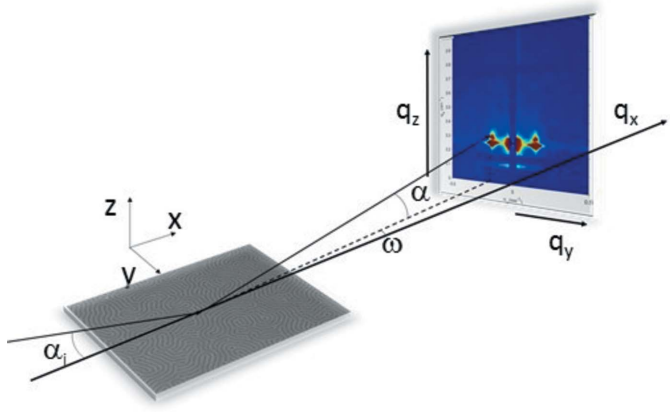

Figure 1
Schematic representation of the GISAXS geometry: a monochromatic X-ray beam hits the sample with an incident angle α_i. The scattered radiation is recorded with a 2D area detector with respect to the α (out-of-plane) and ω (in-plane) exiting angles. The reciprocal-space units (q) represent the scattering wavevector, which depends on the X-ray energy (λ) and the exiting angles (α and ω).

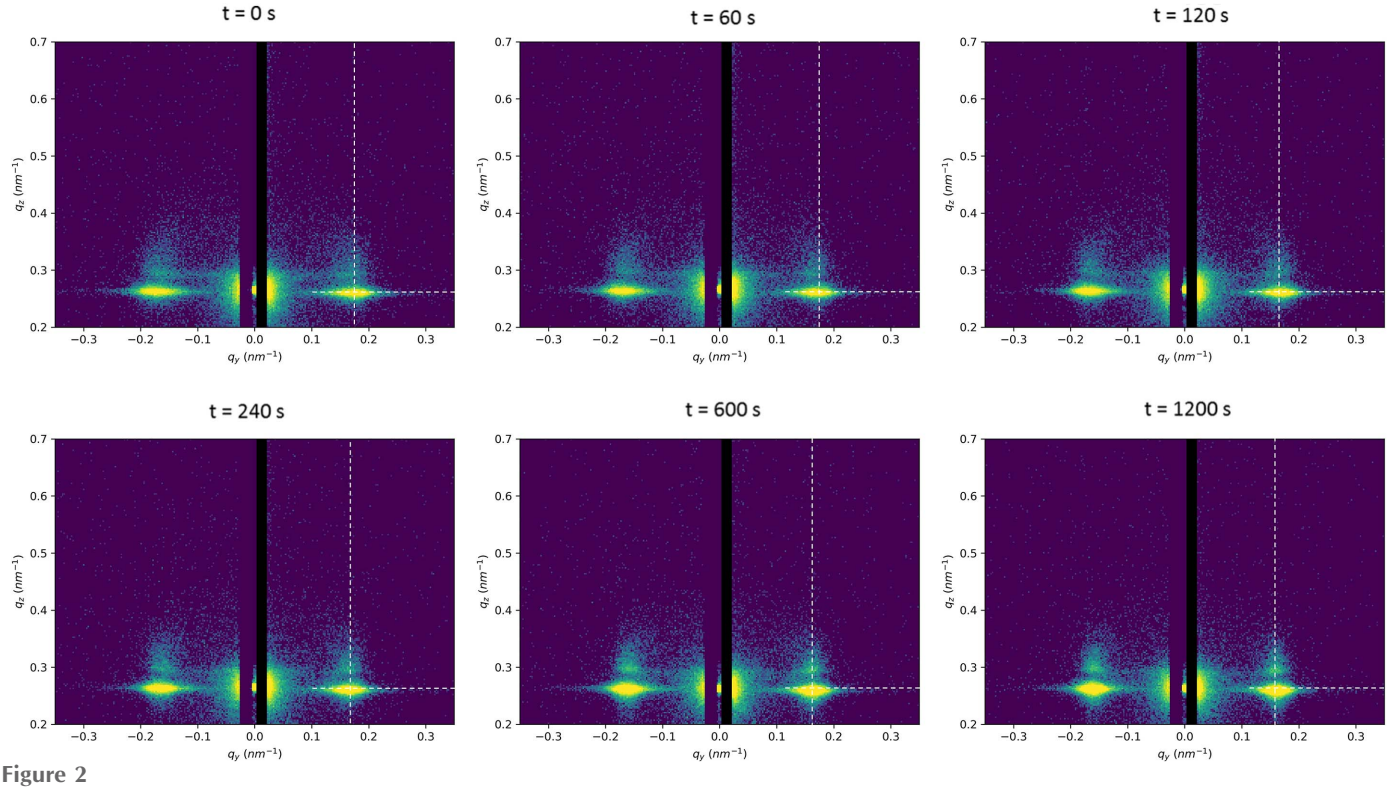

Figure 2
Selection of GISAXS patterns at different processing times during the thermal annealing at 180°C. The dashed vertical and horizontal lines indicate the q_y and q_z main peak position for the further analysis using line cut profiles. After reaching 180°C (t = 0 s) with a ramp rate of 50°C min^{-1}, GISAXS patterns were collected with a frame rate of 1 frame of 37 ms every 60 s. GISAXS patterns showed a clear scattering evolution of the BCP film during the isothermal process: lobe sharpness and the appearance of vertical second-order peaks along q_z were indicative of an increase in the long-range structure of the BCP.

0.251 nm^{-1}), by means of integrating the number of pixels corresponding to a q interval of $q_{z,\mathrm{pos}} \pm 0.01$ nm^{-1}. The main peak q_y position ($q_{y,\mathrm{pos}}$) can be directly related with the average centre-to-centre distances between neighbouring domains, while the peak width is inversely proportional to the correlation length defined as the domain long-range order distance (Förster *et al.*, 2005). In fact, the period of the lamellar structures, L_0, from the $q_{y,\mathrm{pos}}$ can be calculated from the position of the scattering maximum as follows:

$$L_0 = \frac{2\pi m}{q_{y,\mathrm{pos}}}, \tag{2}$$

where m is the order of the reflection (m = 1 for the first scattering peak). The scattering peak q_y maximum position was *circa* 0.165 nm^{-1} which fits with the expected value for a polymer with 38 nm pitch. On the other hand, the grain size (*i.e.* the order of the structure) is inversely proportional to the width of the scattering peak in GISAXS patterns. As the order in the perpendicularly oriented lamellar structures of the BCP film increases, a narrowing of the first-order Bragg peak occurs, concurrent with the eventual appearance of higher-order peaks. The correlation length of a self-assembled BCP can be related to the width of the first-order scattering peak as follows:

$$\xi = \frac{2\pi k}{\mathrm{FWHM}}, \tag{3}$$

where FWHM is the full width at half-maximum of the peak and k is a correction parameter related to the detector type and the fitting of the peak (see Fig. 3). For a 2D detector and a

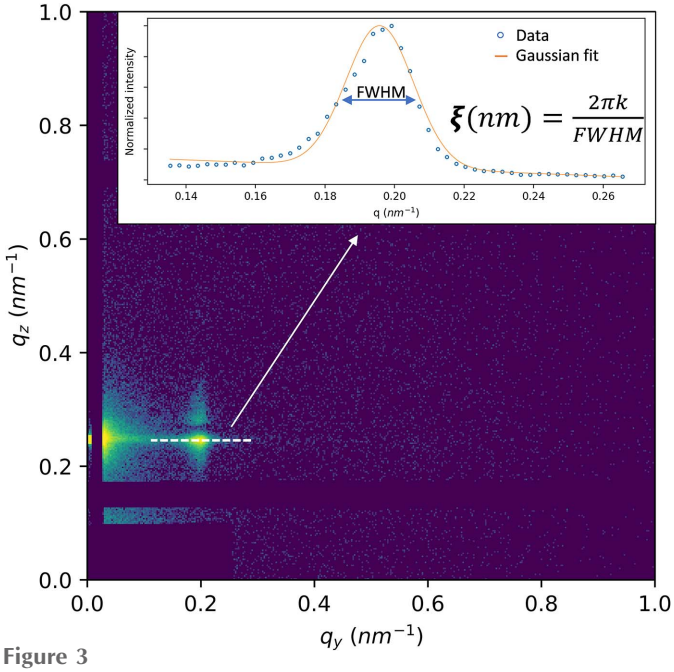

Figure 3
Calculation of the BCP correlation length using a Gaussian fit of the first-order scattering peak.

Gaussian fitting, k has been defined as 0.96 (Smilgies, 2009). In this work, the horizontal cuts in a window of $q_{y,\mathrm{pos}} \pm 0.15$ nm^{-1} were fitted to a Gaussian curve using a MATLAB code prior to the extraction of both the main peak position and FWHM.

3. Experimental results and discussion

3.1. Isothermal annealing of block copolymers

The evolution of the correlation length of BCPs as a function of time under isothermal annealing conditions follows the power-law expression (Harrison *et al.*, 2004; Harrison, Adamson *et al.*, 2000)

$$\xi = A_T\, t^{\phi} \tag{4}$$

where the growth exponent value, ϕ, depends on the polymer material composition as well as the applied annealing conditions. It has a typical value of 0.1–0.3. The parameter A_T depends on the temperature through an Arrhenius behaviour, which can be expressed as $A_T = A_0 \exp(-E_\mathrm{A}/RT)$, where E_A is an activation energy for the self-assembly which depends on the BCP (composition, molecular weight and morphology), R is the ideal gas constant, T is the temperature in Kelvin and A_0 is the pre-exponential factor.

However, equation (4) can only be applied when the self-assembly is strictly occurring during a pure isothermal annealing process or when the target isothermal temperature is reached under rapid annealing conditions, *i.e.* when a negligible evolution of the self-assembly occurs during the short time required for reaching the isothermal temperature. Quantitatively, Perego and co-workers estimated that, in order to assume a rapid thermal annealing (RTA), a heating ramp faster than 18°C s^{-1} is needed (Ferrarese Lupi *et al.*, 2013). Moreover, it has been demonstrated that the final self-assembled film structure of a BCP film is affected both by the presence of intermediate states and by the heating rate (Majewski & Yager, 2015). Therefore, the power-law dependence for BCP self-assembly in equation (4) is not strictly valid under arbitrary annealing conditions and hence a correction factor is required to obtain a precise modelling of the self-assembly evolution.

In fact, the isothermal experiments reported in this work show some polymer ordering occurring during the heating time involved in reaching the annealing temperature. Once the isothermal temperature is reached, the BCP correlation length (ξ_0) is expected to depend on the previous history of the film (heating rate to reach the target temperature, solvent evaporation kinetics *etc.*). In order to include the initial conditions into expression (4), an equivalent time (t_eq) has to be introduced as an offset, which corresponds to the time that the polymer would need to reach the initial observed correlation length under a purely isothermal annealing regime: $\xi_0 = A_T\, t_\mathrm{eq}^{\phi}$. Accordingly, equation (4) can be rewritten as

$$\xi = A_T\big(t + t_\mathrm{eq}\big)^{\phi}. \tag{5}$$

Then, self-assembly kinetics of a BCP during thermal annealing depends on three parameters: the growth exponent (ϕ), the Arrhenius coefficient A_T and the equivalent time (t_eq), which is directly related to the initial correlation length (ξ_0) as $t_\mathrm{eq} = \{[\xi_0(t=0)]/A_T\}^{1/\phi}$. A similar approach is used to model the kinetics of the silicon oxide thermal growth (Deal and Grove model) where the time coordinate is used to account for the presence of an initial oxide layer on the sample (Deal & Grove, 1965).

The analysis of the self-assembly process under isothermal annealing was performed at temperatures from 160 to 190°C, using a heating rate of 50°C min^{-1}, well below the minimum value for being considered RTA. For annealing temperatures lower than 160°C, the BCP self-assembly kinetics are too slow to be efficiently monitored *in situ* by synchrotron experiments, since several hours are needed to observe some polymer order. In contrast, at high annealing temperatures (>190°C) the self-assembly kinetics are fast enough to produce the complete polymer ordering during the heating ramp. Thus, no significant changes were observed in the correlation length during the isothermal annealing from 200°C and above.

During the isothermal annealing, GISAXS patterns correspond to snapshots of the structure and ordering of the BCP. Fig. 2 presents a selection of 2D GISAXS patterns recorded during isothermal annealing at 180°C. GISAXS patterns during isothermal annealing at 160, 170 and 190°C can be found in Figs. S2 to S4. One can observe, first, the formation and, then, the evolution of scattering rods at *circa* q_y = 0.165 nm^{-1} produced by the arrangement of lamellae perpendicular to the sample. From the recorded patterns, the correlation length evolution could be extracted. Fig. 4 depicts the evolution of the q_y horizontal cuts at the Yoneda peak position ($q_{z,\mathrm{pos}}$) versus the annealing time for different temperatures. A detailed view of the evolution of the main scattering peak profiles with annealing time is shown in Fig. S5. As observed, the main scattering peak evolves by increasing its intensity and slightly shifting towards lower q_y values. This characteristic evolution signals an increment of the scattering domain size, indicated by the narrowing of the scattering peak as well as an improved lamella packing, by the reduction of the q_y peak position. As mentioned, to corroborate these findings, the same experiment was repeated several times for each isothermal target temperature (160, 170, 180 and 190°C) (see Fig. 5). An additional experiment was performed by directly placing the sample on the heating stage to produce fast heating for thermal annealing, where the equivalent time would be zero ($t_\mathrm{eq} \simeq 0$).

Isothermal annealing experiments with slow heating rates resulted in a correlation length evolution following the canonical power law [equation (5)]. Table 1 compiles the experimental A_T and ϕ values extracted from the *in situ* data recorded during the annealing experiments. The extracted values (Table 2) were consistent with previously reported investigations for this polymer using SEM defectivity analysis (Claveau, 2018) and for similar polymers (Ji *et al.*, 2011; Majewski & Yager, 2015; Black *et al.*, 2017). As expected, the A_T value increases following an Arrhenius behaviour, the activation energy of the polymer being 29.7 kJ mol^{-1}. Additionally, the ϕ values are within the range of previously

Table 1
Experimental fitting values of BCP kinetic parameters and errors.

T (°C)	ϕ	Error ϕ	A_T (nm)	Error A_T (nm)
160	0.1797	0.0084	30.40	2.09
170	0.1894	0.0062	37.05	1.55
180	0.1931	0.0030	46.46	0.94
190	0.2033	0.0096	52.10	2.95

Table 2
Values of Arrhenius parameters, $A_T = A_0 \exp(-E_A/RT)$, and growth exponent $\phi = \phi_1 + \phi_2 T$ extracted from temperature dependence of block copolymer kinetics.

	Value	Error		Value	Error
A_0 (nm)	1.253×10^5	9.32×10^4	ϕ_1	−0.158	0.0285
E_A (kJ mol^{-1})	29.7	2.3	ϕ_2	7.785×10^{-4}	6.35×10^{-5}

reported values (Black *et al.*, 2017; Perego *et al.*, 2014; Majewski & Yager, 2015; Ferrarese Lupi *et al.*, 2017). It is worth mentioning the existence of a temperature dependence revealed by our experiments (Fig. 6). This dependency can be well described by a linear law, according to the narrow range of temperatures under evaluation: $\phi(T) = \phi_1 + \phi_2 T$. The temperature dependence of A_T and ϕ is shown in Fig. 6 and the fitting parameters are given in Table 2.

3.2. Non-isothermal annealing of block copolymers

The evolution of the BCP lamellar structure under non-isothermal annealing conditions has not been previously studied in as much detail as under isothermal annealing. The modelling of the self-assembly evolution becomes more complex due to the fact that BCP parameters $[A_T(T), \phi(T)]$ are changing during the self-assembly process. Consequently, for the BCP under evaluation, we have extracted the dependence with temperature of both parameters from the isothermal experiments. Thus, we can model their time evolution for any arbitrary thermal treatment for which the temperature is known at each moment. We have implemented an extended model of the self-assembly evolution by dividing the self-assembly process into infinitesimal time intervals, dt, where we can assume that the self-assembly is evolving as under isothermal annealing. A new equivalent time is calculated for each new isothermal interval.

As an example, we have evaluated the particular case of an annealing ramp with a constant heating rate, r, as depicted in Fig. 7. Here, we have divided the annealing time in intervals with a length dt and we have recalculated the parameters $A_T(T)$, $\phi(T)$, t_{eq} for each time interval.

For the first time interval, as in previous isothermal studies, the equivalent time, t_{eq0}, is the one corresponding to the

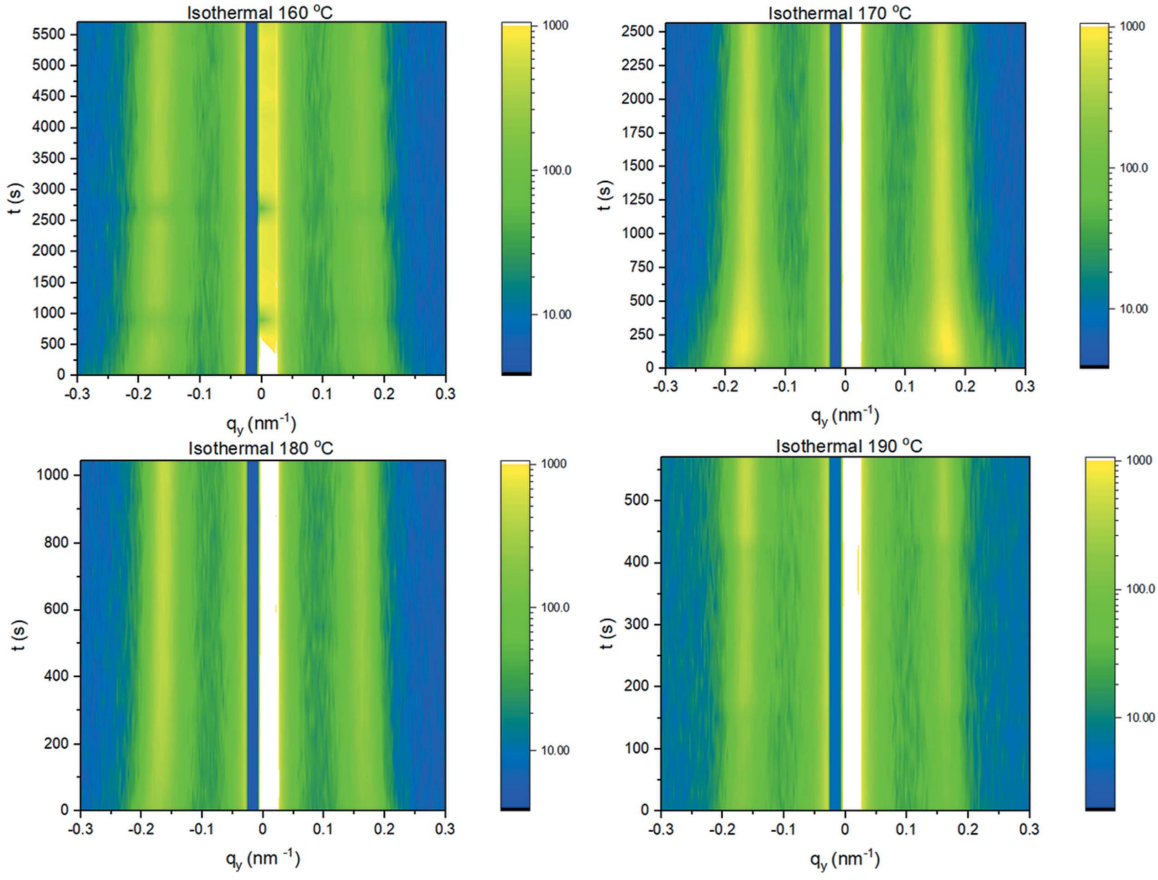

Figure 4
Dynamic evolution of the horizontal line profiles along q_y at the Yoneda peak position during isothermal annealing at different temperatures (160, 170, 180 and 190°C). The colour maps correspond to the intensity of the complete line profile taken at the Yoneda peak q_z position, where the formation and shift towards lower q_y values of the first-order scattering peak were observed.

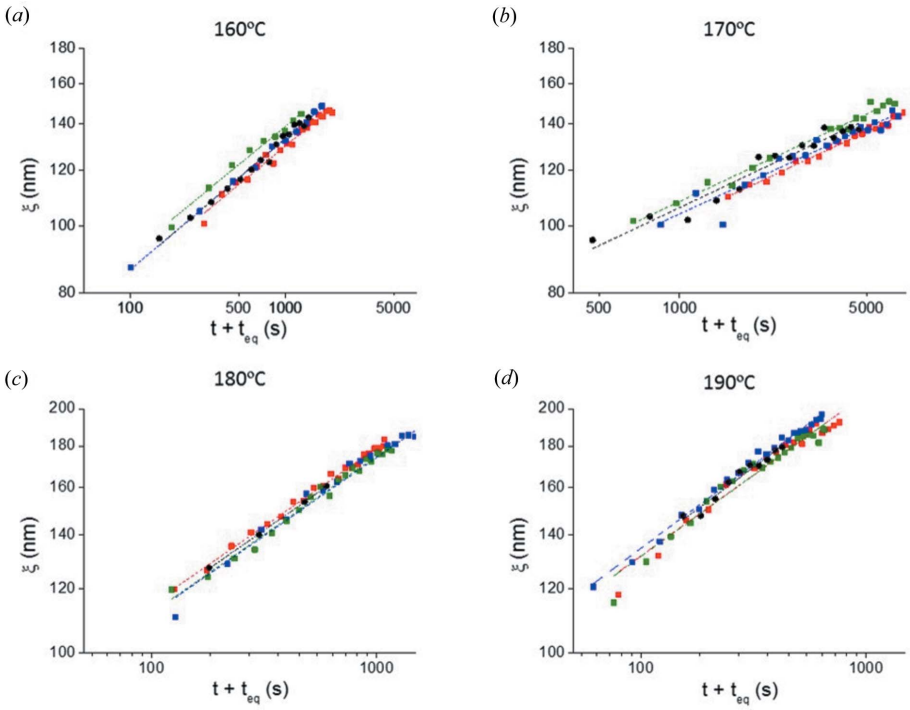

Figure 5
Correlation length evolution as a function of the annealing time at different isothermal treatments (160, 170, 180 and 190°C). Four experiments were performed for each annealing treatment. In the first three experiments (represented by red, blue and green dots) the samples were annealed up to the target temperature using a heating ramp of 50°C min^{-1} while the fourth sample was directly placed on the hot plate at the annealing temperature (represented by black dots).

experimental initial correlation length of the sample, ξ_0, at the initial temperature, T_1:

$$\xi(t=0) = \xi_0 = A_T(T_1)\, t_{eq0}^{(\phi_1+\phi_2 T_1)}, \quad (6)$$

$$t_{eq0} = \left[\frac{\xi_0(t=0)}{A_T(T_1)}\right]^{1/(\phi_1+\phi_2 T_0)}. \quad (7)$$

Then, during the first time interval, $t \in (0, \mathrm{d}t)$, the polymer correlation length evolves as

$$\xi_1(t) = A_T(T_1)(t + t_{eq0})^{(\phi_1+\phi_2 T_1)}. \quad (8)$$

We can recalculate a new equivalent time, t_{eq1-2}, at the end of the first time interval ($t = \mathrm{d}t$) for the evaluation of the polymer correlation length, ξ_2, under the next isothermal temperature, $T_2 = T_1 + \mathrm{d}T = T_1 + r\,\mathrm{d}t$, during the next period from $t \in (\mathrm{d}t, 2\mathrm{d}t)$ by enforcing the continuity of $\xi(t)$:

$$t_{eq1-2} = \left[\frac{\xi_1(\mathrm{d}t)}{A_T(T_2)}\right]^{1/(\phi_1+\phi_2 T_2)}, \quad (9)$$

$$\xi_2(t) = A_T(T_2)(t + t_{eq1-2})^{(\phi_1+\phi_2 T_2)}. \quad (10)$$

A straightforward recalculation of the modified correlation length and the corresponding equivalent time for each interval of time n, under a new isothermal temperature $T_n = T_1 + nr\,\mathrm{d}t$, leads to

$$\xi_n(t) = A_T(T_n)[t + t_{eq(n-1)-n}]^{[\phi_1+\phi_2(T_n)]}, \quad (11)$$

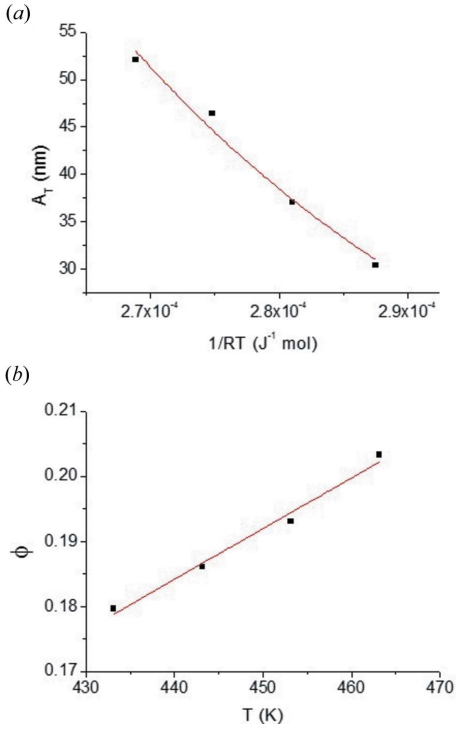

Figure 6
BCP kinetic parameter dependence with temperature: (*a*) Arrhenius dependence of A_T parameter evolution as a function of temperature, (*b*) exponential parameter temperature dependence. As a first approach we have assumed a linear dependence with temperature ($\phi = \phi_1 + \phi_2 T$).

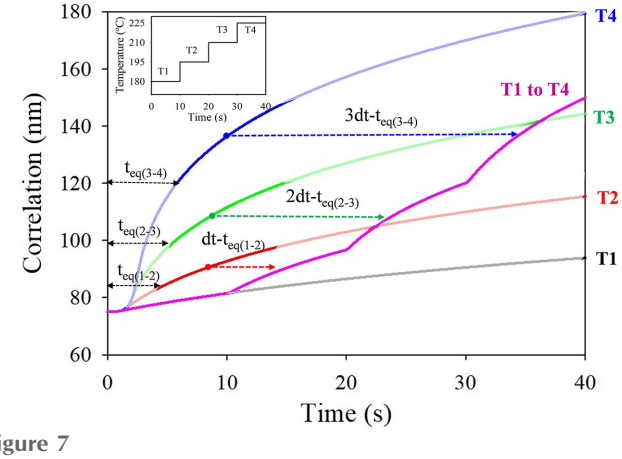

Figure 7
Modelling of the non-isothermal annealing. This figure illustrates the procedure to determine the evolution of the correlation length when the annealing temperature is not constant. To clarify the process, in this example the ramp temperature has a step-like form with time steps of 10 s, as shown in the inset. The heating rate for the model is 90°C min^{-1} and the initial and final temperatures are 180°C and 215°C, respectively. At each step, the evolution follows that of an isothermal annealing but translated by a certain time (t_{eq}) to ensure the continuity of the actual correlation length.

$$t_{\mathrm{eq}(n-1)-n} = \left\{\frac{\xi[(n-1)\,\mathrm{d}t]}{A_T(T_n)}\right\}^{1/(\phi_1+\phi_2 T_n)}. \qquad (12)$$

Fig. 7 depicts graphically the result of consecutive application of equations (11) and (12): the mathematical modelling is equivalent to translating a segment of the isothermal curve (red, green and blue curves) by a time equal to t_{eq} to fit to the value of the correlation length on the non-isothermal curve (pink curve) at the initial time of the interval dt. In the figure dt is set to 10 s for clarity. When modelling real experiments at a constant heating rate, the interval of time, dt, is set small enough to assume that during each time the system evolves under isothermal conditions, preventing the introduction of any significant error. For samples analysed in this paper, the heating ramp is divided into 1000 isothermal steps, which corresponds to dt values between 0.0025 s and 0.01 s. Then, the time correlation length evolution is solved numerically using equations (6) to (10) by implementing a MATLAB routine.

The structural evolution of the BCP lamellar structure was obtained for different heating rates (5, 10 and 20°C min^{-1}). Samples were placed after the spin-coating step on the heating stage and heated to the target temperature of 180°C. Then, after reaching the final temperature of 180°C, the polymer was annealed under isothermal conditions for a few minutes. The initial temperature of the heating ramp for the studies was chosen to be 150°C which is the temperature at which polymer evolution starts to be observed (see Fig. S6). At a lower temperature, the evolution of the correlation length is difficult to evaluate due to low intensity and the width of the peaks which makes the Gaussian fit difficult. The BCP kinetics are also very slow and the effect of the annealing on the BCP order is not observed at low temperatures (see Fig. S6). Additionally, the initial order present in the samples at 150°C can be mainly attributed to the evaporation of the remaining PGMEA solvent on the film, which takes place during the spin-coating and the first minutes of the heating ramp. This effect is especially important in these experiments due to the slow heating rates used during the ramp.

Fig. 8 shows the experimental correlation length versus the time at the final temperature obtained from the collected GISAXS patterns during the *in situ* characterization for non-isothermal experiments. Initial correlation lengths on samples at t = 0 (150°C) are different due to the previous thermal history of each sample. Samples were heated from room temperature to 150°C by using a ramp of 5, 10 and 20°C min^{-1}. Then, the sample with a slower heating ramp has a higher initial correlation length because of the longer thermal history.

It can be observed that low heating rates require higher time at the isothermal final temperature to achieve the final lamellar structure. These experimental data were compared with the predicted values using the proposed model (Fig. 8). The results show that the model predicts satisfactorily the obtained experimental values for the three heating rates investigated. It is worthwhile remarking that there are no fitting parameters in the modelling: the values of A_T and ϕ obtained from the isothermal characterization are considered.

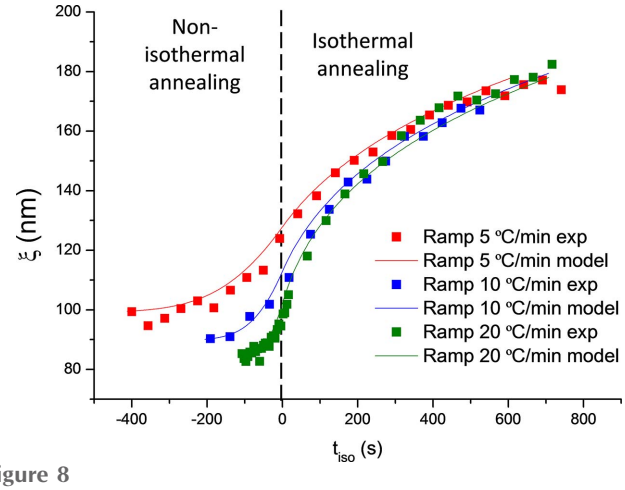

Figure 8
Correlation length time evolution during a heating ramp, at 5°C min^{-1} (red), 10°C min^{-1} (blue) and 20°C min^{-1} (green), from 150 to 180°C followed by isothermal annealing at 180°C. The time origin (t = 0) is defined as the beginning of the isothermal annealing. Experimental values are represented by dots and the evolution predicted by the mathematical model [equations (11) and (12)] by lines.

After the mathematical model verification, we are able to predict how the annealing conditions, heating rate and initial correlation length influence the kinetics of the self-assembly process. Figs. 9(*a*) and 9(*c*) illustrate the evolution of the correlation length during the thermal annealing at 1°C s^{-1} to 180°C and 230°C, respectively, as a function of the initial polymer correlation length. Results show that for short isothermal annealing times, and especially at the lower temperatures (180°C), there is a clear influence of the initial correlation length, indicating that the previous history of the polymer plays a role in the correlation length evolution. Complementarily, Figs. 9(*b*) and 9(*d*) present the evolution of the correlation length for different temperature ramp rates for a constant initial correlation length of 90 nm. The model shows a clear dependence of the correlation length evolution with the final target temperature as well as with the heating rate employed. It is observed that a pure isothermal evolution (which would correspond to a constant slope in the figures, as they are represented in log–log form) is only obtained for a significant amount of time after the heating ramp has finished.

As a consequence the extraction of BCP kinetic parameters using the classical approach, $\xi = A_T\, t^{\phi}$, is only valid for a pure isothermal annealing, where the target temperature has been quasi-instantaneously reached, or using a fast thermal annealing. We have compared the calculation of ϕ using the classical approach (see Fig. S7) with the accurate modelling that we have presented (Fig. 10). When ϕ is estimated using the classical approach on samples previously annealed with a relatively slow heating rate, the obtained value is lower than the real one, and it is only reached after a long annealing time. Consequently, in order to reach an accurate value of ϕ the experiment must consider a long enough annealing time under isothermal conditions. The minimum annealing time under isothermal conditions depends on the annealing temperature and on the heating rate.

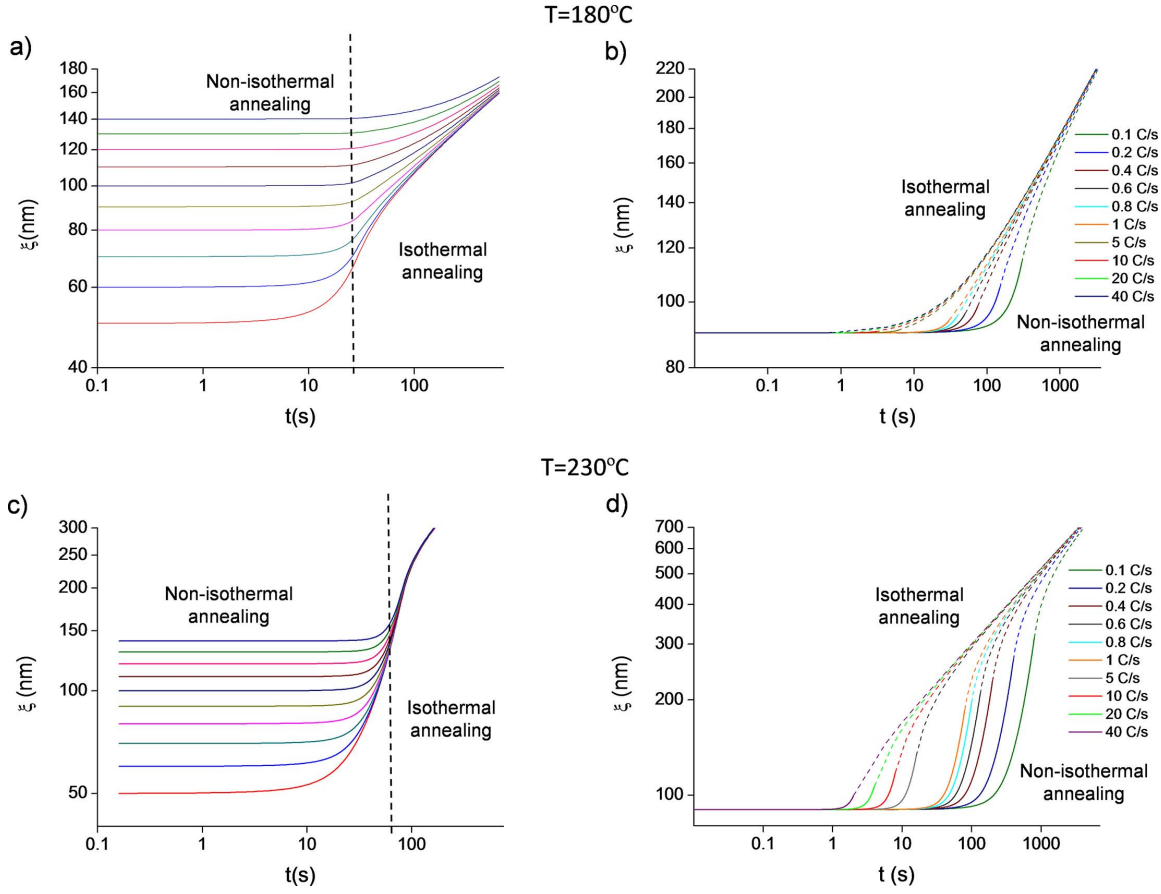

Figure 9
Modelling of correlation length evolution for a BCP from 150°C to the target temperature 180°C (top) and 230°C (bottom). The figures on the left [(*a*) and (*c*)] illustrate the influence of the initial correlation length. The annealing is performed first with a temperature ramp of 1°C s^{-1} and then isothermal annealing once the target temperature is reached, as indicated by the vertical line. For the figures on the right [(*b*) and (*d*)], the BCP film is annealed using different temperature ramp rates (from 0.1°C s^{-1} to 40°C s^{-1} and then kept at constant temperature for a few min). The initial correlation length is 90 nm. All ramps start at t = 0 s. The correlation length during the ramp is represented by solid lines and dashed lines when the isotherm is reached.

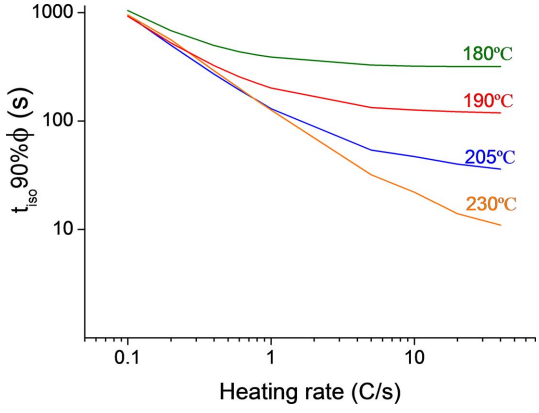

Figure 10
Isothermal annealing time required to achieve a 90% accuracy of the correlation length growth exponent, ϕ, when the initial correlation length is not considered. The calculation is performed for four different temperatures and for a range of heating rates from 0.1 to 40°C s^{-1} during the non-isothermal annealing. The correlation length was estimated using the model described in the article that takes into account the equivalent time, t_{eq}. Time equal to zero corresponds to the starting time of the isothermal annealing. All the samples were heated from 150°C to the target temperature (180, 205, 215 and 230°C) at different heating rates. The initial correlation length is set to 90 nm for all the curves.

4. Conclusions

The analysis of the kinetics of the structural order in lamellar structures of BCPs using GISAXS allows access to statistical information over relatively large areas as compared with standard microscopy techniques. GISAXS characterization has the additional advantage that it is compatible with the self-assembly annealing experimental conditions usually employed in DSA processing, allowing for the *in situ* and real-time characterization of BCP ordering.

However, for data interpretation and in order to take into account non-ideal experimental conditions, the classical modelling for BCP kinetics needs to be adapted. We have introduced a new parameter, the equivalent time, which enables the analysis of the evolution of the correlation length independently of the previous thermal history of the sample, caused for example by solvent evaporation or slow heating ramps. This approach can be used to reproduce the evolution of the correlation length in non-isothermal annealing. The model has been validated during different heating ramps but could be applied to any system where the temporal dependence of temperature is known.

Finally, we have demonstrated that, in order to obtain an accurate estimation of the parameters that determine the BCP self-assembly kinetics, the equivalent time should be considered when analysing the experimental data from the real-time experiments. This effect is particularly important for samples undergoing a slow heating rate or annealed at low temperature if accurate values of the kinetics parameters need to be obtained.

Acknowledgements

GISAXS experiments were performed at the NCD-SWEET beamline at the ALBA Synchrotron with the collaboration of ALBA staff.

Funding information

This project has received funding from the European Union's Horizon 2020 research and innovation programme under the Marie Skłodowska-Curie grant agreement No. 665919, the Spanish Ministry of Economy and Competitiveness (MINECO) under contract Nos. MAT2015-68307-P, MAT2015-66443-C02-1-R, TEC2015-69864-R, RTI2018-102007-B-I00, PID209-107514GB-100, RYC-2016-21412 and the Generalitat de Catalunya under contract No. 2017 SGR 1187. The ICN2 is funded by the CERCA program/Generalitat de Catalunya. The ICN2 is supported by the Severo Ochoa Centres of Excellence programme, funded by the Spanish Research Agency (AEI, grant No. SEV-2017-0706) (MINECO/FEDER, UE).

References

Bates, C. M., Maher, M. J., Janes, D. W., Ellison, C. J. & Willson, C. G. (2014). *Macromolecules*, **47**, 2–12.
Bates, F. & Fredrickson, G. H. (1990). *Annu. Rev. Phys. Chem.* **41**, 525–557.
Berezkin, A. V., Jung, F., Posselt, D., Smilgies, D. M. & Papadakis, C. M. (2018). *Adv. Funct. Mater.* **28**, 1–15.
Berry, B. C., Bosse, A. W., Douglas, J. F., Jones, R. L. & Karim, A. (2007). *Nano Lett.* **7**, 2789–2794.
Black, C. T., Forrey, C. & Yager, K. G. (2017). *Soft Matter*, **13**, 3275–3283.
Chandra, A., Nakatani, R., Uchiyama, T., Seino, Y., Sato, H., Kasahara, Y., Azuma, T. & Hayakawa, T. (2019). *Adv. Mater. Interfaces*, **6**, 1–7.
Claveau, G. (2018). PhD thesis, Université Grenoble Alpes, France.
Deal, B. E. & Grove, A. S. (1965). *J. Appl. Phys.* **36**, 3770–3778.
Di, Z., Posselt, D., Smilgies, D. M. & Papadakis, C. M. (2010). *Macromolecules*, **43**, 418–427.
Evangelio, L., Fernández-Regúlez, M., Fraxedas, J., Müller, M. & Pérez-Murano, F. (2019). *Appl. Mater. Interfaces*, **11**, 3571–3581.
Fernández-Regúlez, M., Evangelio, L., Lorenzoni, M., Fraxedas, J. & Pérez-Murano, F. (2014). *Appl. Mater. Interfaces*, **6**, 21596–21602.
Ferrarese Lupi, F., Giammaria, T. J., Ceresoli, M., Seguini, G., Sparnacci, K., Antonioli, D., Gianotti, V., Laus, M. & Perego, M. (2013). *Nanotechnology*, **24**, 315601.
Ferrarese Lupi, F., Giammaria, T. J., Seguini, G., Laus, M., Dubček, P., Pivac, B., Bernstorff, S. & Perego, M. (2017). *Appl. Mater. Interfaces*, **9**, 11054–11063.
Förster, S., Timmann, A., Konrad, M., Schellbach, C., Meyer, A., Funari, S. S., Mulvaney, P. & Knott, R. (2005). *J. Phys. Chem. B*, **109**, 1347–1360.
Gottlieb, S., Kazazis, D., Mochi, I., Evangelio, L., Fernández-Regúlez, M., Ekinci, Y. & Perez-Murano, F. (2018). *Soft Matter*, **14**, 6799–6808.
Gottlieb, S., Lorenzoni, M., Evangelio, L., Fernández-Regúlez, M., Ryu, Y. K., Rawlings, C., Spieser, M., Knoll, A. W. & Perez-Murano, F. (2017). *Nanotechnology*, **28**, 175301.
Gottlieb, S., Rösner, B., Evangelio, L., Fernández-Regúlez, M., Nogales, A., García-Gutiérrez, M. C., Keller, T. F., Fraxedas, J., Ezquerra, T. A., David, C. & Perez-Murano, F. (2018). *Mol. Syst. Des. Eng.* **4**, 175–185.
Gu, X., Gunkel, I., Hexemer, A., Gu, W. & Russell, T. P. (2014). *Adv. Mater.* **26**, 273–281.
Hahm, J. & Sibener, S. J. (2001). *J. Chem. Phys.* **114**, 4730–4740.
Harrison, C., Adamson, D. H., Cheng, Z., Sebastian, J. M., Sethuraman, S., Huse, D. A., Register, R. A. & Chaikin, P. M. (2000). *Science*, **290**, 1558–1560.
Harrison, C., Angelescu, D. E., Trawick, M., Cheng, Z., Huse, D. A., Chaikin, P. M., Vega, D. A., Sebastian, J. M., Register, R. A. & Adamson, D. H. (2004). *Europhys. Lett.* **67**, 800–806.
Harrison, C., Chaikin, P. M., Huse, D. A., Register, R. A., Adamson, D. H., Daniel, A., Huang, E., Mansky, P., Russell, T. P., Hawker, C. J., Egolf, D. A., Melnikov, I. V. & Bodenschatz, E. (2000). *Macromolecules*, **33**, 857–865.
Harrison, C., Cheng, Z., Sethuraman, S., Huse, D. A., Chaikin, P. M., Vega, D. A., Sebastian, J. M., Register, R. A. & Adamson, D. H. (2002). *Phys. Rev. E.*, **66**, 1–27.
Hu, H., Gopinadhan, M. & Osuji, C. O. (2014). *Soft Matter*, **10**, 3867–3889.
IRDS (2018). *International Roadmap for Devices and Systems* (IRDS), 2018 edition. New York: IEEE. (https://irds.ieee.org/.)
Jeong, S. J., Kim, J. Y., Kim, B. H., Moon, H. S. & Kim, S. O. (2013). *Mater. Today*, **16**, 468–476.
Ji, S., Liu, C. C., Liao, W., Fenske, A. L., Craig, G. S. W. & Nealey, P. F. (2011). *Macromolecules*, **44**, 4291–4300.
Jung, Y. S. & Ross, C. A. (2009). *Adv. Mater.* **21**, 2540–2545.
Kim, B., Laachi, N., Delaney, K. T., Carilli, M., Kramer, E. J. & Fredrickson, G. H. (2014). *J. Appl. Polym. Sci.* **131**, 40790.
Lee, S., Cheng, L. C., Yager, K. G., Mumtaz, M., Aissou, K. & Ross, C. A. (2019). *Macromolecules*, **52**, 1853–1863.
Li, W. & Müller, M. (2016). *Prog. Polym. Sci.* **54–55**, 47–75.
Lorenzoni, M., Evangelio, L., Fernández-Regúlez, M., Nicolet, C., Navarro, C. & Pérez-Murano, F. (2017). *J. Phys. Chem. C*, **121**, 3078–3086.
Magerle, R. (2000). *Phys. Rev. Lett.* **85**, 2749–2752.
Majewski, P. W. & Yager, K. G. (2015). *Soft Matter*, **12**, 281–294.
Marencic, A. P. & Register, R. A. (2010). *Annu. Rev. Chem. Biomol. Eng.* **1**, 277–297.
Maret, M., Tiron, R., Chevalier, X., Gergaud, P., Gharbi, A., Lapeyre, C., Pradelles, J., Jousseaume, V., Fleury, G., Hadziioannou, G., Boudet, N. & Navarro, C. (2014). *Macromolecules*, **47**, 7221–7229.
Müller-Buschbaum, P. (2016). *Eur. Polym. J.* **81**, 470–493.
Murphy, J. N., Harris, K. D. & Buriak, J. M. (2015). *PLoS One*, **10**, e0133088.
Papadakis, C. M., Di, Z., Posselt, D. & Smilgies, D.-M. (2008). *Langmuir*, **24**, 13815–13818.
Perego, M., Ferrarese Lupi, F., Ceresoli, M., Giammaria, T. J., Seguini, G., Enrico, E., Boarino, L., Antonioli, D., Gianotti, V., Sparnacci, K. & Laus, M. (2014). *J. Mater. Chem. C*, **2**, 6655–6664.
Renaud, G., Lazzari, R. & Leroy, F. (2009). *Surf. Sci. Rep.* **64**, 255–380.
Rueda, D. R., Martín-Fabiani, I., Soccio, M., Alayo, N., Pérez-Murano, F., Rebollar, E., García-Gutiérrez, M. C., Castillejo, M. & Ezquerra, T. A. (2012). *J. Appl. Cryst.* **45**, 1038–1045.
Samant, S., Strzalka, J., Yager, K. G., Kisslinger, K., Grolman, D., Basutkar, M., Salunke, N., Singh, G., Berry, B. & Karim, A. (2016). *Macromolecules*, **49**, 8633–8642.
Sanz, A., Rueda, D. R., Ezquerra, T. A. & Nogales, A. (2011). *J. Nanostruct. Polym. Nanocomposites*, **7**, 10–17.

Segal-Peretz, T., Winterstein, J., Doxastakis, M., Ramírez-Hernández, A., Biswas, M., Ren, J., Suh, H. S., Darling, S. B., Liddle, J. A., Elam, J. W., de Pablo, J. J., Zaluzec, N. J. & Nealey, P. F. (2015). *ACS Nano*, **9**, 5333–5347.
Sepe, A., Hoppe, E. T., Jaksch, S., Magerl, D., Zhong, Q., Perlich, J., Posselt, D., Smilgies, D. M. & Papadakis, C. M. (2011). *J. Phys. Condens. Matter*, **23**, 254213.
Sinturel, C., Grosso, D., Boudot, M., Amenitsch, H., Hillmyer, M. A., Pineau, A. & Vayer, M. (2014). *Appl. Mater. Interfaces*, **6**, 12146–12152.
Smilgies, D.-M. (2009). *J. Appl. Cryst.* **42**, 1030–1034.
Soccio, M., Alayo, N., Martín-Fabiani, I., Rueda, D. R., García-Gutiérrez, M. C., Rebollar, E., Martínez-Tong, D. E., Pérez-Murano, F. & Ezquerra, T. A. (2014). *J. Appl. Cryst.* **47**, 613–618.
Tseng, Y. C. & Darling, S. B. (2010). *Polymers (Basel)*, **2**, 470–489.
Yager, K. G., Fredin, N. J., Zhang, X., Berry, B. C., Karim, A. & Jones, R. L. (2009). *Soft Matter*, **6**, 92–99.
Zhang, J., Posselt, D., Smilgies, D.-M., Perlich, J., Kyriakos, K., Jaksch, S. & Papadakis, C. M. (2014). *Macromolecules*, **47**, 5711–5718.